Article

pubs.acs.org/Biomac

Influence of Molecular Structure on the In Vivo Performance of Flexible Rod Polyrotaxanes

Christopher J. Collins,[†] Yawo Mondjinou,[†] Bradley Loren,[†] Sandra Torregrosa-Allen,[‡,§] Christopher J. Simmons,[†] Bennett D. Elzey,[‡,§] Nadia Ayat,[∥] Zheng-Rong Lu,[∥] and David Thompson*[,†,‡,⊥]

[†]Department of Chemistry, Purdue University, Multi-disciplinary Cancer Research Facility, 1203 W. State Street, West Lafayette, Indiana 47907, United States

[‡]Purdue University Center for Cancer Research, 201 S. University Street, West Lafayette, Indiana 47907, United States

[§]Department of Comparative Pathobiology, Purdue University, 625 Harrison Street, West Lafayette, Indiana 47907, United States

[∥]Department of Biomedical Engineering, Case Western Reserve University, 10900 Euclid Avenue, Cleveland, Ohio 44106, United States

[⊥]Weldon School of Biomedical Engineering, Purdue University, 206 S. Martin Jischke Drive, West Lafayette, Indiana 47907, United States

Supporting Information

ABSTRACT: Polyrotaxanes, a family of rod-shaped nanomaterials comprised of noncovalent polymer/macrocycle assemblies, are being used in a growing number of materials and biomedical applications. Their physiochemical properties can vary widely as a function of composition, potentially leading to different in vivo performance outcomes. We sought to characterize the pharmacokinetic profiles, toxicities, and protein corona compositions of 2-hydroxypropyl-β-cyclodextrin polyrotaxanes as a function of variations in macrocycle threading efficiency, molecular weight, and triblock copolymer core structure. We show that polyrotaxane fate in vivo is governed by the structure and dynamics of their rodlike morphologies, such that highly threaded polyrotaxanes are long circulating and deposit in the liver, whereas lung deposition and rapid clearance is observed for species bearing lower 2-hydroxypropyl-β-cyclodextrin threading percentages. Architecture differences also promote recruitment of different serum protein classes and proportions; however, physiochemical differences have little or no influence on their toxicity. These findings provide important structural insights for guiding the development of polyrotaxanes as scaffolds for biomedical applications.

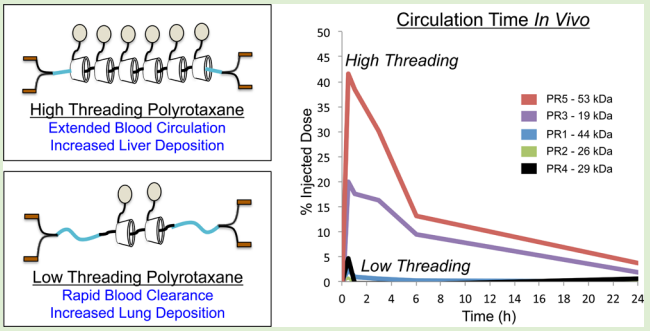

INTRODUCTION

Nanoparticle (NP) vehicles hold considerable potential for biomedical applications in drug delivery, diagnostic imaging, and vaccine development using lipids,[1] polymers,[2] or metals[3] to generate NPs with a variety of sizes, shapes, and surface chemistries.[4] There is a growing awareness that the physical and chemical properties of the material plays a major role in determining its residence time, toxicity, and biological fate upon in vivo administration.[4−7] Given our limited understanding of how material properties affect their in vivo performance, there is significant benefit to studying structure−property relationships between NP classes to determine how changes in their composition will affect their biological performance.

Effective clinical translation requires a deep understanding of the pharmacokinetics (PK), biodistribution (BD), and pharmacodynamics of the NP system. Immediately after injection into the bloodstream, the NP encounters a vast spectrum of serum proteins, blood cells, the immune system, and other cellular components all having the potential to influence NP PK and BD, as well as initiate NP-mediated side effects.[8,9] A wide range of toxic effects may result from these interactions, including red blood cell (RBC) lysis, thrombogenesis, or complement activation, processes that can contribute to anemia, renal failure, stroke, and inflammatory responses.[9−11] Additionally, NP with different physical characteristics are known to have different organ deposition and clearance pathways.[12,13] Information about clearance and biodistribution can guide both the targeting of specific organs for therapy or imaging and the monitoring of organ specific toxicity. Once within the organs, they have the potential to induce toxic effects if they are not cleared effectively, as seen with carbon nanotubes[14] and quantum dots.[15,16] Knowing the types of physical and chemical characteristics that lead to

Received: April 8, 2016
Revised: July 1, 2016
Published: July 7, 2016

DOI: 10.1021/acs.biomac.6b00508
Biomacromolecules 2016, 17, 2777−2786

predictable toxicities and biodistribution patterns will inform the use of NP vehicles for drug delivery or imaging applications.

The protein corona bound to NP is emerging as a major determinant of their in vivo fate.[17] Protein deposition onto NP occurs immediately upon exposure to serum with the corona composition remaining relatively stable over time.[18,19] The protein mixtures within these coronas has the potential to influence their PK, BD, and clearance rate.[20] Varied architectures have been shown to differentially recruit corona proteins, including serum albumins, immunoglobulins, and complement proteins and in many cases recruit them in different abundances.[10,20−22] Knowledge of the factors influencing NP protein corona deposition will go a long way toward explaining or predicting their in vivo performance.

Polyrotaxanes (PR) are a unique class of rod-shaped nanomaterials derived from a noncovalent macrocycle threading process onto an included polymeric core. Bulky blocking groups prevent macrocycle dethreading until PR end-cap cleavage from the polymer termini.[23] They are of great interest because they can be made from biocompatible, biodegradable, or generally recognized as safe starting materials,[24−26] as recently exemplified by the use of Pluronic copolymers and β-cyclodextrin derivatives to prepare PR for applications in gene delivery, Niemann-Pick Type C (NPC) disease, and magnetic resonance imaging (MRI).[26−30]

Beyond their characterization as MRI contrast agents, only two studies using tumor bearing mice and single PR architectures have been reported with biodistributions occurring predominantly in the liver.[31,32] Additional studies showing PR biocompatibility with blood components (e.g., platelets, fibrinogen, and albumin) in vitro, anticoagulant activity (e.g., inhibition of platelet cytoplasmic calcium increase and an increased clot formation time), and reduced fibrinogen binding to polyurethane surfaces with PR modification[33−35] have been reported; however, no data are available with regard to the PK, BD, and toxicity of PR materials as a function of their molecular and supramolecular structure. Understanding this relationship is crucially important because PRs can be synthesized with a vast diversity of polymer precursors and macrocycle types, and molar ratios can produce variations in PR average molecular weights, macrocycle copy numbers, and threading efficiencies that may dramatically affect their biological performance.

To address this shortcoming in our understanding of PR in vivo performance, we sought to develop a PR structure−property relationship by synthesizing a family of Gd^{3+}/1,4,7,10-tetraazacyclododecane-1,4,7-trisacetic acid-10-benzylisothiocyanate (DO3A)-modified 2-hydroxypropyl-β-cyclodextrin (HP-β-CD) PR from a set of poly(ethylene)glycol/poly(propylene)-glycol/poly(ethylene glycol) (PEG−PPG−PEG, Pluronic) triblock copolymers of varying molecular weights and hydrophilic/lipophilic ratios (Figure 1c).[24] We found that the PR molecular weight, threading efficiency, rodlike character, and core polymer hydrophilicity have major impacts on PK, BD, toxicity, immune response, and protein corona composition.

EXPERIMENTAL SECTION

Materials. HP-β-CD and Pluronic copolymers were purchased from Sigma-Aldrich. Polymer average molecular weights and hydrophilic−lipophilic balances were determined by the manufacturer. Claritas PPT grade gadolinium standard was purchased from Fisher Scientific. TraceMetal grade nitric acid was purchased from Thermo Fisher Scientific. All dilutions were made with either 18 MΩ water or 2% HNO_3 in 18 MΩ water.

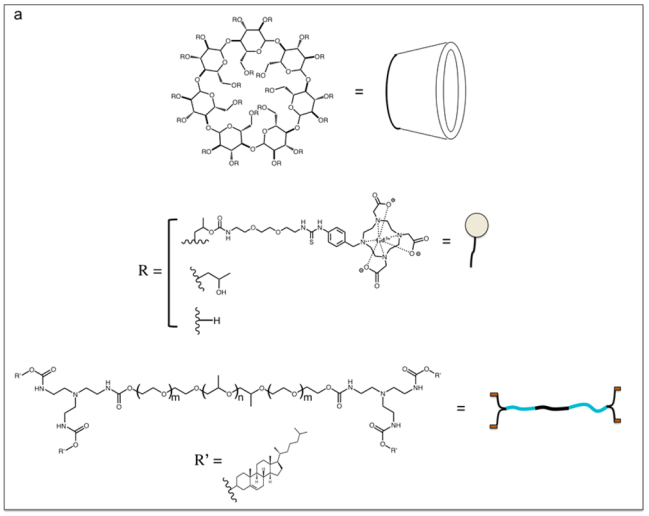

c

Polymer Core Characteristics

Base	MW	PEG	PPG	HLB
F127	12.5 kDa	200	65	22
F68	8.3 kDa	151	29	29
L35	1.9 kDa	21	16	19
L64	2.9 kDa	26	30	15
L81	2.8 kDa	6	43	2

Polyrotaxane Characteristics

PR	Total MW	# CDs	% Threading	Gd Wt %
PR1	44 kDa	14	44%	22
PR2	26 kDa	3	20%	66
PR3	19 kDa	4	50%	10
PR4	29 kDa	6	40%	14
PR5	53 kDa	14	67%	4.3

Figure 1. PR physicochemical properties. (a) PR component molecular structures. m = half the given number of PEG block units, n = number of PPG units. (b) Representative structures of each member of the PR family. (c) Polymer core and PR physiochemical characteristics.

Polyrotaxane Synthesis, Modification, and Purification. Gd^{3+}/DO3A HP-β-CD PR were synthesized and purified as previously described.[29,30] Briefly, Pluronic copolymer termini were modified with α,ω-bis-tris(2-aminoethyl)amino] groups before HP-β-CD threading. To affect the threading reaction, bis-amine modified polymers were suspended in hexane and sonicated until homogeneous. Subsequently, HP-β-CD was added to the reaction mixture, bath sonicated for 1 h, probe sonicated for 10 min, and stirred vigorously for 72 h. End-cap addition was achieved by the removal of hexane and addition of cholesteryl chloroformate in CH_2Cl_2. Final products were purified by precipitation in diethyl ether and dialysis against either 12−14 or 6−8 kDa regenerated cellulose membranes depending on the initial molecular weight of the copolymer core. Materials were dialyzed initially against DMSO and secondarily against H_2O before lyophilization. We have previously shown that this process is effective in removing unreacted starting materials, typically reducing the levels of unthreaded CD to <5%.[27,29,30] This process gave initial PR starting materials which were subsequently modified to carry Gd^{3+}/DO3A.

PR modification was achieved by activation with 1,1′-carbonyldiimidazole before coupling with 1,8-diamino-3,6-dioxooctane. These products were again purified by dialysis against DMSO and H_2O for 3 d before lyophilization. Subsequently, 8-diamino-3,6-dioxooctane modified PR were dissolved in DMSO before addition of p-SCN-Bn-DO3A. Again, an identical dialysis purification process was utilized before lyophilization. Finally, Gd^{3+} complexation was performed by stirring DO3A-modified PR with $GdCl_3{\cdot}6H_2O$ for 48 h at pH 5.5−6.5. Final products were purified by dialysis against H_2O (pH 7) for 3 d to remove unchelated Gd^{3+}.

Polyrotaxane Characterization. NMR characterization was done using a Bruker DRX500 500 MHz NMR with a QNP probe and

DOI: 10.1021/acs.biomac.6b00508
Biomacromolecules 2016, 17, 2777−2786

DMSO-d_6 as solvent. The Pluronic methyl peak was integrated to the average of protons for the given polymer with all additional peaks assigned relative to this standard. Estimation of the average number of HP-β-CDs resident on a given PR was done by comparing the integrals of the HP-β-CD H-1 peak and the Pluronic core methyl group. It is known that threaded β-cyclodextrins will preferentially occupy the Pluronic hydrophobic PPG core.[36] Threading efficiencies were calculated for each PR based on the total number HP-β-CDs which could be threaded given a PPG/CD ratio of 2:1. Percent threading is given as a percent of a theoretical 100% coverage. For analysis of gadolinium content, ~1 mg samples of each PR were dissolved in 70% HNO_3 at a concentration of 2 mg/mL. Samples were allowed to digest overnight. Each PR solution was then diluted to a concentration of 10 ppb Gd^{3+} based on the theoretical amount expected based on NMR integration of the DOTA peaks. The final nitric acid concentration of all samples was 2%.

In Vivo Studies of Pharmacokinetics and Biodistribution. Male Balb/c mice were purchased from Harlan Laboratories (Indianapolis, IN) and allowed to acclimate for 2 weeks before PR administration. Injection was done at 9 weeks of age with mice weighing 21−24 g. Isoflurane gas was used for anesthesia. All experiments were performed under an approved protocol from the Purdue Animal Care and Use Committee.

PR were solubilized in sterile DMSO and sonicated for 10 min before dilution to 15% DMSO with sterile PBS to give a final PR concentration of 2 mg/mL. Each PR was administered via tail vein in a 100 μL injection to a group of six mice. Blood draws of ~50 μL were taken at 0, 0.5, 1, 3, and 6 h after administration for pharmacokinetic analysis. At 24 h, mice were sacrificed and the liver, spleen, kidney, lungs, heart, and brain tissues were dissected for ex vivo analysis of biodistribution. Organs were weighed and snap frozen in LN_2. Blood, serum, and organs were all stored at −80 °C until analysis.

Sample Digestion for Inductively Coupled Mass Spectrometry (ICP-MS) Analysis. Blood and serum (5−20 μL) were typically digested by addition of 70% HNO_3 (100 μL). HNO_3 mixtures were incubated at 80 °C for 16 h to give pale yellow solutions before dilution to 5−8 mL to give a final HNO_3 content of 2%. Organ and feces samples were thawed, sectioned, weighed and homogenized before digestion with 100−200 μL HNO_3 at 80 °C for 16−48 h. Livers, brains, and kidneys required longer digestion times than did lungs, spleens, and hearts. After digestion, hearts and brains were diluted to 5 mL volumes. Spleens and kidneys were diluted to 5 mL volumes and then further by 1:10. Lungs samples were diluted to 10 mL volumes and further by 1:10. Livers were diluted to 10 mL volumes and further by another 1:15. All final solutions were filtered through 0.2 μm PTFE syringe filters (Macherey-Nagel, Bethlehem, PA). Final HNO_3 concentrations of all samples was 2%.

Inductively Coupled Plasma Mass Spectrometry (ICP-MS) Analysis. The ^{156}Gd and ^{158}Gd inductively coupled argon plasma mass spectrometry (ICPMS) results were obtained using an ELEMENT-2 (ThermoFinnigan, Bremen, Germany) mass spectrometer with a Netbuie data system upgrade in the medium resolution mode to minimize interferences. $R = M/\Delta M \sim 3500$. In order to prevent magnet shifts with time, the mass offset program was used with the ^{40}Ar ^{40}Ar peak at m/z 79.7242 as the locked mass. The argon sweep gas and nitrogen of the Aridus was adjusted for maximum peak height and stability using ^{7}Li, ^{115}In, and ^{238}U peaks obtained from a Merck multielement standard (1 ng/mL, Merck & Co.). (^{115}In typically has $1-2 \times 10^6$ cps in the low resolution mode and 80 000−100 000 cps in the medium resolution mode.) Typical sweep gas values were 2.5−3.5 L/min for argon and 16−20 L/min for nitrogen. The tuning peaks were enhanced by adjusting the lenses. A calibration was then performed.

A 10 ppb Gd standard was used (Exaxol, Clearwater, FL) to determine the mass offsets and the ^{40}Ar ^{40}Ar was set as the locked mass peak. The samples were introduced into the plasma using an Aridus desolvating system with a T1H nebulizer (Teledyne Cetac, Omaha NE), which is used to enhance sensitivity and reduce oxide and hydride interferences. The sample uptake rate was approximately 60 μL/min with an argon nebulizer gas flow rate of 1 L/min. The spray chamber was heated to 80 °C to help reduce the formation of solvent droplets. An ASX-100 autosampler (Teledyne Cetac, Omaha, NE) was used. Each sample was scanned with 3 runs and 30 passes with a wash time of 2 min and a take up time of 1 min.

PR Excretion. During the performance of the pharmacokinetics experiments, feces samples were collected to follow the excretion of PR materials as they cleared from the body. At selected intervals, feces were collected from the cage. Pooled feces produced by three mice in each group were collected for the 0−2 h and 2−6 h time periods and homogenized mechanically before digestion and analysis. At 24 h, each of the three mice were placed on individual Petri dishes; the spontaneously produced feces were collected from each individual for analysis.

Calculations. Percent injected dose calculations are based on the experimentally determined Gd^{3+} load of each PR, a concentration of 2 mg/mL PR, an injection volume of 100 μL, and an average total blood volume of 78 mL/kg.[37]

Anti-PEG IgG Antibody Production and Body Weight Analysis. A second set of three mice per group was used to probe for the production of anti-PEG antibodies after challenge with the PR constructs. All groups contained three mice and were challenged once with 100 μL 2 mg/mL PR injections at day 0. Blood (~50 μL) was collected at day 14 and screened for anti-PEG IgG antibodies. On day 14, groups treated with PR3, PR4, and PR5 were rechallenged with an additional 100 μL PR injection. At day 21, mice were sacrificed, blood was collected by cardiac blood draw, and blood was allowed to clot and was separated by centrifugation before serum analysis by ELISA. For body weight analysis, all animals were weighed before injection and subsequently at days 1, 5, 9, 14, and 21. Values are presented as average body weight ± SEM.

Enzyme-Linked Immunosorbant Assays. ELISA studies for antibody production were done using a Mouse Anti-PEG IgG ELISA kit purchased from Life Diagnostics, Inc. (West Chester, PA) and were conducted according to the manufacturers protocol. Briefly, serum was diluted 1:100 or 1:50 and added to a BSA-PEG coated 96-well plate in duplicate. After incubation for 1 h, secondary antimouse IgG-HRP conjugate was added before incubation for 45 min. Final TMB substrate incubation for 20 min was followed by addition of stop solution and quantifying absorption of the plate at 450 nm with correction at 570 nm.

Serum Chemistry. Terminally drawn 21 day serum samples from animals in the antibody production study were pooled (150 μL each mouse) for each PR group. Mean values for the groups were determined for ALT, ALKP, creatinine, blood urea, electrolytes, and blood CO_2. Analysis was performed by the Purdue Veterinary Teaching Hospital Clinical Pathology Lab (West Lafayette, IN). Samples were run on a Vitros 5,1 FS from Ortho Clinical Diagnostic (Rochester, NY) per the manufacturer's protocols. Normal blood chemistry levels for Balb/C mice were obtained from Charles River research models (http://www.criver.com/files/pdfs/rms/balbc/rm_rm_r_balb-c_mouse_clinical_pathology_data.aspx).

Hemolysis Assay. Human red blood cells (RBCs) were purchased from Zen-Bio, Inc. (Research Triangle Park, NC) and stored at 4 °C until use. RBCs were washed 4 times with 150 mM NaCl and subsequently diluted 1:50 before testing. Each PR or starting material was dissolved in DMSO and sonicated for 15 min before dilution with PBS and sonication for an additional 15 min. Final DMSO concentrations were 1%. PRs were then serially diluted in 1% DMSO to give solutions of 800, 100, and 20 μg/mL. Aliquots of washed RBCs (190 μL) were then incubated with 10 μL PR for 1 h at 37 °C. Final PR concentrations were 40, 5, and 1 μg/mL with final DMSO concentrations of 0.05%. Final concentrations for HP-β-CD were 300, 150, and 50 μM. Final concentrations for Pluronic copolymers were 50, 25, and 5 μM. Triton X-100 (1%) was used as a positive control. After incubation, cells were pelleted by centrifugation for 5 min at 600g and 100 μL of supernatant was collected. All experiments were done in triplicate. Hemolysis was analyzed using a Nanodrop ND-1000 (Thermo Scientific, Wilmington DE) by probing released hemoglobin absorption at 415 nm. Control

DOI: 10.1021/acs.biomac.6b00508
Biomacromolecules 2016, 17, 2777−2786

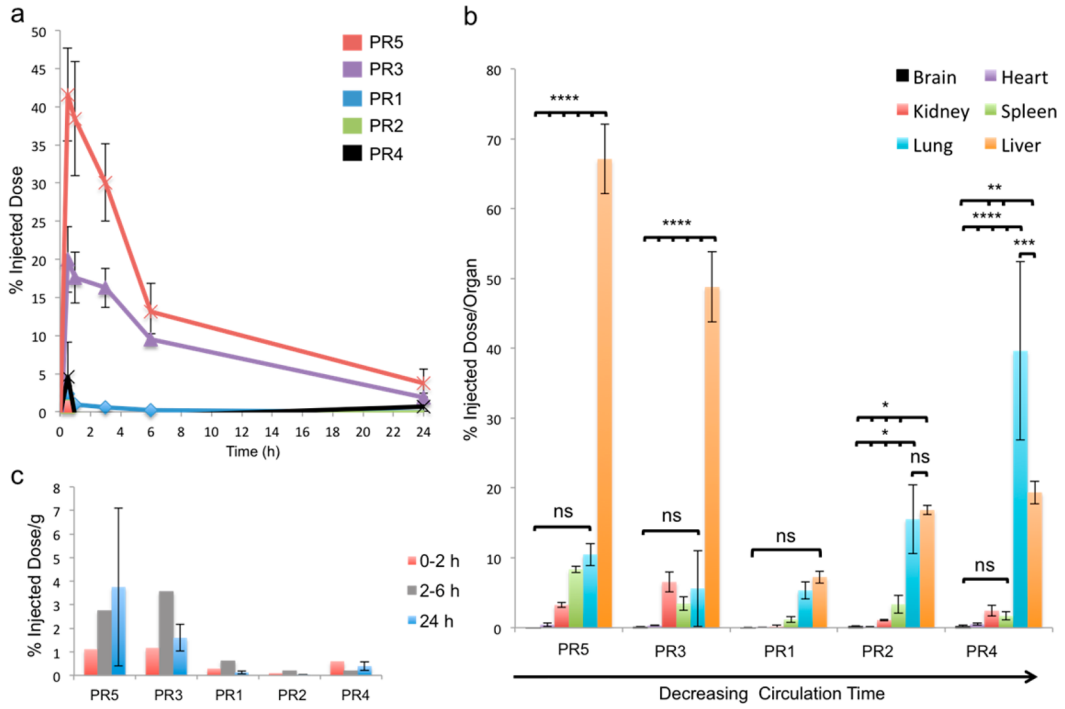

Figure 2. Pharmacokinetics of PR derivatives. (a) Blood circulation time as determined by ICP-MS detection of Gd^{3+} content in blood. For PR1, PR3, and PR4, $n = 6$. For PR2, $n = 5$. For PR5, $n = 3$. (b) PR biodistribution as determined by ICP-MS detection of Gd^{3+} content in tissue homogenates. In all cases, $n = 6$, except PR1 heart and PR4 brain where $n = 5$. (c) PR clearance via the biliary route. Data for time periods between 0 and 2 h and 2 and 6 h are pooled means; data was collected from individual mice at 24 h ($n = 3$). *$p < 0.05$, **$p < 0.01$, ***$p < 0.005$, ****$p < 0.001$.

experiments were run using a Biotek Neo plate reader (Winooski, VT). Results were normalized to the Triton X-100 positive control.

Protein Corona Analysis. Normal human serum was purchased from Complement Technology, Inc. (Tyler, TX) and thawed immediately before use. PR (100 μg) were taken up in PBS and bath sonicated for 10 min before incubation with undiluted human serum (1:1 v/v) for 1 h at 37 °C. After incubation, samples were centrifuged for 10 min at 4000*g* and PR pellets were washed four times with 150 μL cold PBS. Three separate incubations were done for each PR species.

Tryptic peptides were separated on a nanoLC system (1100 Series LC, Agilent Technologies, Santa Clara, CA). The peptides were loaded on an Agilent 300SB-C18 enrichment column (5 × 0.3 mm, 5 μm) for concentration prior to switching the enrichment column into the nanoflow path after 5 min. Peptides were separated with the Agilent C18 reversed phase ZORBAX 300SB-C18 analytical column (0.75 μm × 150 mm, 3.5 μm). The column was connected to an emission tip (New Objective) and coupled to the nanoelectrospray ionization (ESI) source of a high-resolution hybrid ion trap mass spectrometer LTQ-Orbitrap XL (Thermo Scientific). The peptides were eluted from the column using acetonitrile (ACN)/0.1% formic acid (FA) (mobile phase B) linear gradient. For the first 5 min, the column was equilibrated with 95% H_2O/0.1% FA (mobile phase A), followed by the linear gradient of 5% B to 40% B in 65 min at 0.3 μL/min, then from 40% B to 100% B for an additional 10 min. The column was washed with 100% of ACN/0.1% FA and equilibrated with 95% of H_2O/0.1% FA before the next sample was injected (total method time = 95 min). A blank injection was run between each sample to avoid carryover.

The LTQ-Orbitrap mass spectrometer was operated in the data-dependent positive acquisition mode in which each full MS scan (30,000 resolving power) was followed by eight MS/MS scans; the eight most abundant molecular ions were selected and fragmented by collision induced dissociation using a normalized collision energy of 35%. Activation time was 30 ms, capillary temperature was 200 °C, source voltage was 1.2 kV, capillary voltage was 35 V, and tube lens was 100 V. To enable the detection and fragmentation of a representative number of ions, dynamic exclusion was used during primary peptide selection. If an ion was detected within the eight most abundant molecular ions in two scans within 30 s, it was dynamically excluded for 60 s.

Database searching was conducted using MaxQuant Label Free Quantitation (LFQ) and Intensity Based Absolute Quantitation (iBAQ) The human (SwissProt) annotated database was used for the search. Initial Spectral Counting was performed using the Mascot Database search results. Statistical analysis (multiregression analysis) was performed using Qlucore software package and LFQ intensities.

Magnetic Resonance Imaging. PR relaxivity measurements were acquired on a Bruker 7T small animal scanner. Relaxivity of PR materials at increasing concentrations were acquired using MSME and RARE pulse sequences. A single scan was acquired for each material.

Statistics. Significance of biodistribution, anti-PEG production, and proteomic analysis was assessed by two-way ANOVA and Tukey's multiple comparisons test using Graphpad Prism (La Jolla, CA). All values are presented as mean ± s.e.m. *$p < 0.05$, **$p < 0.01$, ***$p < 0.005$, ****$p < 0.001$.

RESULTS AND DISCUSSION

Gd^{3+}/PR Family Characterization. Five Pluronic cores (F127, F68, L35, L64 and L81) were chosen across a wide range of average molecular weights (12.5−1.9 kDa) and varying hydrophilic−lipophilic balances (HLBs) (Figure 1c). These polymer precursors were selected to maximize differences in starting material architecture across these criteria. Copolymers F127 and F68 allowed the effects of increasing PPG block length and absolute molecular weight to be studied at higher masses. The remaining copolymers (L35, L64, and L81) were selected to represent a low molecular weight regime with L35 being only 1.9 kDa and span HLBs from overall hydrophilic to strongly hydrophobic. Comparison between the two groups

DOI: 10.1021/acs.biomac.6b00508
Biomacromolecules 2016, 17, 2777−2786

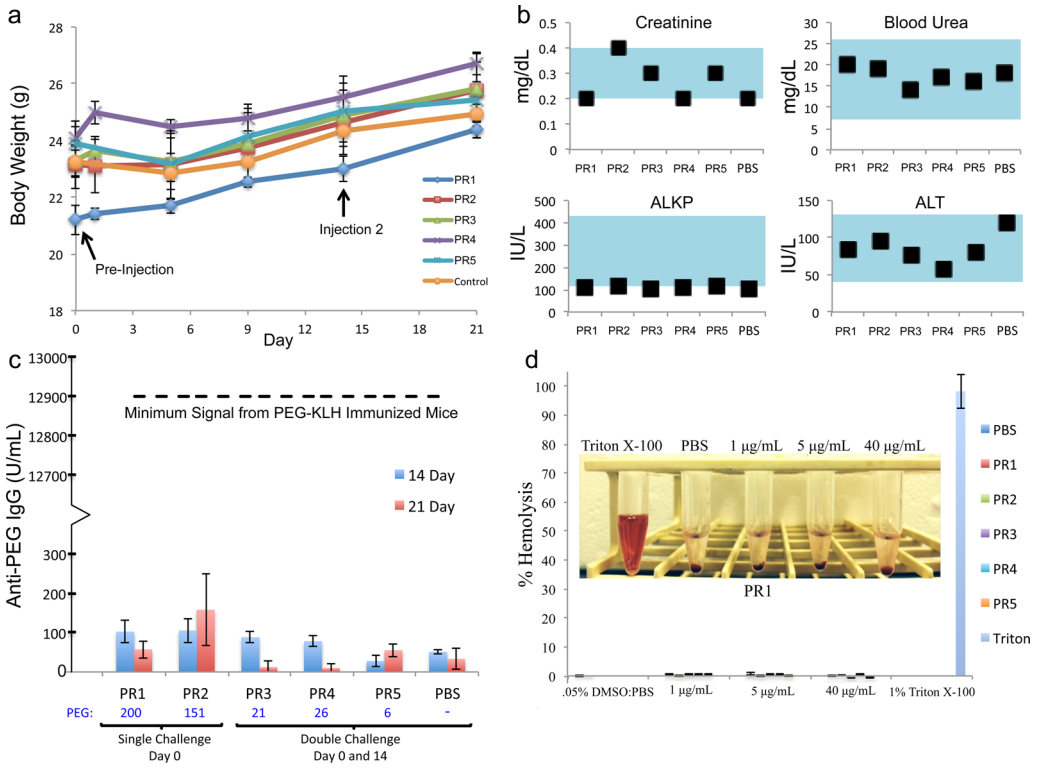

Figure 3. Acute toxicity of PR1−PR5. (a) Mice treated with different PR gain weight similarly to vehicle treated controls. $n = 3$. (b) Serum chemistry biomarkers for kidney (top) or liver (bottom) damage are unchanged relative to PBS controls. Typical creatinine, BUN, ALKP, and ALT ranges for BALB/c mice (Harlan Laboratories) are shown in blue. (c) Anti-PEG IgG production is similar to PBS control after single and double PR challenge. Note break in *Y*-axis. Dotted line signifies the minimum anti-PEG IgG signal given by PEG-KLH immunized mice.[41] $n = 3$. (d) No significant human red blood cell hemolysis was noted upon incubation with PR1−PR5. $n = 3$.

allowed for the study of precursor polymer molecular weight and PEG block length effects in both synthesis and biological performance.

Gd^{3+}/DO3A-modified PR were prepared, purified, and analyzed by ^1H NMR to determine the average molecular weight and threading efficiency of the PR family members (Figures S1−5).[29,30] Average molecular weights ranged from 53 to 19 kDa and average HP-*β*-CD threading efficiencies ranged from 67% to 20% depending on the PR type (Figure 1). These values are averages, as the PR materials exist as a distribution of polymer molecular weights carrying a distribution of HP-*β*-CD copy numbers. At increased threading efficiencies, we expect the Gd^{3+}/DO3A PR materials to adopt flexible rodlike conformations as we have previously shown through atomic force microscopy analysis of similar materials.[30] Threading efficiency is defined as the percent coverage of the central PPG core block and is calculated as a ratio of the average number of threaded HP-*β*-CDs obtained to the number of HP-*β*-CDs required for complete coverage.

The most highly threaded PR, PR5, is also the highest molecular weight, despite having a low molecular weight core (L81), due to the presence of 14 threaded copies of HP-*β*-CD. We attribute the high threading of this polymer to its larger central PPG block and reduced interference from the short PEG blocks that enable a more efficient threading reaction. The most hydrophilic polymer chosen, F68, produced a PR (PR2) with the lowest threading efficiency (20%). In contrast to the L81 case, the hydrophilicity of F68 (HLB = 29) retarded HP-*β*-CD threading relative to the other polymers of lower HLB. The highest MW polymer core, F127, gave rise to the second highest molecular weight PR (PR1), although with a significantly lower HP-*β*-CD threading efficiency (44%) than for PR5, likely due to chain end entanglement within the lengthy PEG blocks. Finally, Pluronic L35 produced a PR with the lowest MW and second highest threading (PR3).

This set of materials was then studied to gain insight into the roles of PR physiochemical properties on their biological behavior. The range of threading efficiencies in the materials allowed for the elucidation of threading and rigidity effects on performance. In addition, the total HP-*β*-CD copy number range (14−3 CDs) may reveal differences in the effects based simply on greater HP-*β*-CD loadings. Comparison of PR1 and PR4 would be informative in this case, as they have similar threading efficiencies despite a large difference in HP-*β*-CD copy number. In addition, comparison of PR3 and PR5 would allow for comparison of highly threaded PRs with large differences in HP-*β*-CD copy number. The PR also exhibited a large range of molecular weights, beneficial for determining the effects of total mass on performance. The properties of PR1 and PR5 allowed for comparison of high molecular weight PR derived from polymer precursors of vastly different masses and PEG block lengths and their influence on PR fate in vivo. This family of PR materials, however, allowed us to probe many aspects of PR design space and draw conclusions about which properties are most deterministic to biological performance.

Pharmacokinetics, Biodistribution, and Clearance. We sought to determine how the different PR architectures would influence PR circulation times, biodistribution, and clearance upon tail vein injection into BALB/c mice. The blood circulation profiles are shown in Figure 2a. All members of the PR family displayed biphasic kinetics with rapid and slower clearance phases. Circulation times appear to be most affected

DOI: 10.1021/acs.biomac.6b00508
Biomacromolecules 2016, 17, 2777−2786

by the threading extent of the PR PPG core. PR5, with the highest threading and the highest molecular weight, was the longest circulating PR, with an average of 41.6% of the injected dose remaining in the blood at 30 min, 13.1% remaining at 6 h, and 3.8% remaining at 24 h. The second longest circulating construct, PR3, had 20% of the injected dose remaining at 30 min, 9.5% at 6 h, and 1.9% at 24 h. This is a revealing case because PR3 exhibits the second highest threading and the lowest overall molecular weight, yet displays long circulation properties. These findings reveal that PPG block coverage and flexible rodlike characteristics may be more important than overall PR molecular weight for long circulation. PR1 was only slightly retained in blood (44% threading efficiency; ~1% of the injected dose at 1 h; ~0.2% at 6 h), while PR2 and PR4 with threading efficiencies of 20% and 40%, respectively, were both undetectable in blood circulation after 1 h. Expansion of PK profiles for PR1, PR2, and PR4 is available in Figure S6.

We infer from these PK data that PPG block coverage by HP-β-CD is more important for increasing circulation time than overall molecular weight due to a rotaxanation-induced increase in rigidity of the PR to produce a more rodlike structure.[38] Similar results have been reported for flexible rod PEG−PCL micelles that display long circulation properties by aligning with blood-flow and avoiding macrophage uptake.[5] Slow PR clearance from blood is likely not due to PEG shielding effects since the longest circulating agent, PR5, has the shortest PEG blocks (average of 3 units on each side), while the PRs with the longest PEG blocks (PR1 and PR2) are rapidly cleared.

PR biodistribution at 24 h is also strongly influenced by PR threading efficiency. Each PR accumulates to some extent in both kidney and spleen; however, no structure−property trend is discernible. There is little to no detectable PR residence in the brain or heart (Figure 2b). The more highly threaded PRs showed deposition in the liver preferentially to all other organs. PR5 and PR3 showed liver deposition of 67.1% ID/organ and 48.8% ID/organ, respectively, while PR2 and PR4 showed deposition of <20% ID in this organ in both cases (Figure 2b). Correspondingly, the more highly threaded PRs were excreted in greater average amounts through the feces than those with lower degrees of threading (Figure 2c). PR with low threading efficiencies are deposited more extensively in lung (Figure 2b), with PR4 showing greater deposition in lung (39.7% ID/organ) than liver (Figure 2b). Greater lung deposition by PR with lower threading efficiencies may be due to PR aggregation via their partially exposed PPG blocks. These aggregates, driven by the amount of available hydrophobic core, could then be too large to effectively pass through microcapillaries of the lungs.

PR biodistribution and excretion profiles are largely in contrast to those previously described for HP-β-CD. Upon intravenous administration, nearly the entirety of the injected HP-β-CD dose is found unmetabolized in the urine at 24 h.[39] Biodistribution and excretion, therefore, is dominated by renal filtration, whereas PR all deposit in the liver and feces to varying degrees. In 49-day old mice, 90% of the dose is cleared completely from the body within 6 h.[40] This is, again, in contrast to PR, which in the case of PR1, PR3, and PR5 can still be found circulating in the blood at 6 h and are resident in the organs at 24 h.

Toxicity and Blood Compatibility. PR systemic toxicity was then evaluated by measuring the body weights of PR treated groups over a 3 week treatment course (Figure 3a). All groups of 9-week old mice received an initial PR injection at day 0. Additionally, groups treated with PR3, PR4, and PR5 were challenged a second time with an injection at day 14. With termination of the experiment at day 21, all groups were within the weight limits for 12-week-old mice, indicating that PR treatment did not exhibit acutely toxic effects in mice.

Blood chemistry tests were performed as indicators of liver, kidney, and lung function after PR challenge. Equal volumes of mouse serum collected 21 d after PR injection were pooled for each group to obtain mean values (Figure 3b). Blood creatinine and blood urea nitrogen (BUN) were within normal limits for BALB/c mice, suggesting no evident kidney toxicity. This is an important finding since renal elimination is the major route of clearance for PR1, PR2 and PR4. It is also relevant to the potential use of Gd^{3+}:DO3A-PR as MRI contrast agents, since renal damage is a significant concern for currently approved Gd^{3+} contrast agents.[42]

Additionally, alkaline phosphatase (ALKP) and alanine transaminase (ALT) enzymes were studied as markers of liver damage (Figure 3b). ALT was within normal limits, indicating no evident liver damage after PR challenge. ALKP was low or slightly below normal limits in most cases, including the PBS control. The fact that liver damage would be expected to elevate ALKP values suggests that the potential for PR mediated liver toxicity is low. Blood CO_2 (ECO_2) was used as a marker of potential lung toxicity caused by PR deposition. In all cases, PR treated groups had ECO_2 values similar to PBS controls, indicating no acute lung toxicity (Figure S7). Additional serum chemistry values are available in Figures S8 and 9. These studies are in agreement with previous studies showing that monomeric HP-β-CD is well tolerated and further shows that rotaxanation of the macrocycle does not generate acute toxicity.[43]

One of the most important aspects of blood compatibility is the effect of an injected NP on circulating RBCs. NP-mediated RBC lysis can lead to a lack of oxygen delivered to the tissues, oxidative damage to the vascular endothelium, and kidney impairment over time.[44] Increasing concentrations of PR incubated with human RBCs showed no evidence of hemolysis compared to PBS control (Figure 3d). This is in contrast to certain PR starting materials, including HP-β-CD and the Pluronic surfactants (e.g., L81 and L35), which generate small, but statistically significant hemolysis levels relative to PBS controls (Figure S10) at the concentrations present during PR incubation. It appears, then, that rotaxanation is able to mitigate the undesirable hemolytic properties exhibited by HP-β-CD.

Interaction of PR constructs with components of the immune system will have a major impact on their clearance rate, metabolism, and biodistribution.[45] Of particular importance for applications requiring repeated injections or long-term administration (e.g., drug delivery, MRI, or NPC therapeutics) is the production of memory immunoglobulin G (IgG) antibodies to antigens present on the PR surface. Activation of an IgG response would limit the utility of PR for repeated administration by initiating rapid PR clearance upon reinjection.[46] PEGylated NP surfaces have previously been shown to induce the production of anti-PEG IgG,[46] therefore, we sought to determine whether the PR PEG blocks would elicit production of this antibody.

Anti-PEG IgG production was tested 14 and 21 d after injection of the PR materials. (Figure 3c). At 14 d, groups of mice that were administered PR3, PR4, and PR5 were rechallenged with a second injection before termination of the experiment at 21 d. At no point in the experiment were

DOI: 10.1021/acs.biomac.6b00508
Biomacromolecules 2016, 17, 2777−2786

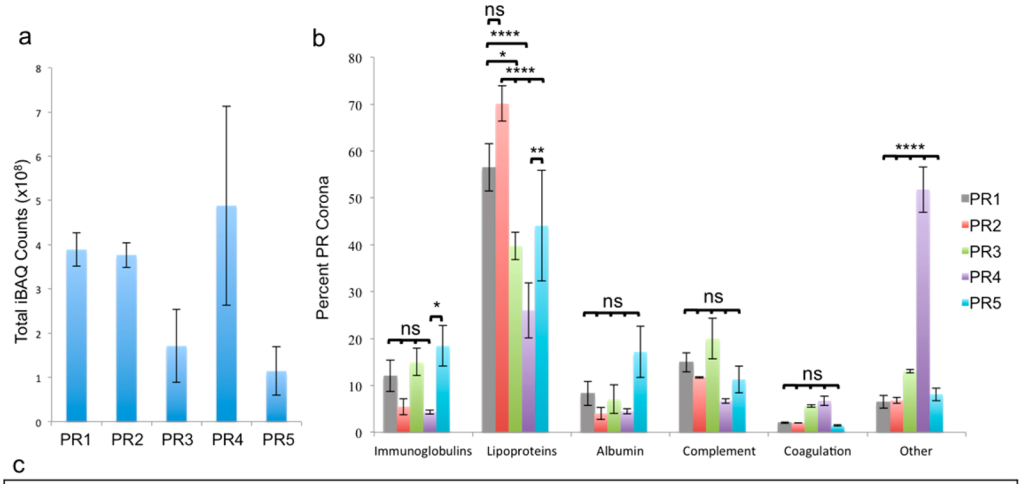

c

	PR1 (73.9%)	PR2 (80.5%)	PR3 (63.4%)	P4 (73.5%)	PR5 (74.2%)
1	Apolipoprotein A-I	Apolipoprotein A-I	Vitronectin	Transthyretin	Serum albumin
2	Complement C3	Apolipoprotein A-II	Apolipoprotein C-III	Apolipoprotein C-III	Apolipoprotein C-III
3	Serum albumin	Apolipoprotein C-III	Serum albumin	Apolipoprotein A-I	Apolipoprotein A-I
4	Apolipoprotein A-II	Apolipoprotein C-II	Apolipoprotein C-II	Prothrombin	Ig kappa chain C region
5	Apolipoprotein C-III	Apolipoprotein C-I	Apolipoprotein A-II	Serum albumin	Apolipoprotein C-I
6	Apolipoprotein C-I	Complement C3	Ig kappa chain C region	Apolipoprotein C-II	Complement C3
7	Apolipoprotein C-II	Alpha-2-HS-glycoprotein	Hyaluronan-binding protein 2	Apolipoprotein A-IV	Apolipoprotein C-II
8	Ig kappa chain C region	Serum albumin	Complement C3	Hyaluronan-binding protein 2	Ig gamma-1 chain C region
9	Apolipoprotein E	Apolipoprotein E	Apolipoprotein A-I	Vitronectin	Clusterin
10	Ig gamma-1 chain C region	Apolipoprotein A-IV	Clusterin	Inter-alpha-trypsin inhibitor heavy chain H2	Apolipoprotein E

Figure 4. PR corona proteomics. (a) Total protein deposition and (b) protein corona composition are affected by changes in PR physiochemical properties. $n = 3$ biological replicates. (c) List of top 10 most abundant corona proteins. Percentage indicates the corona ratio occupied by the 10 most abundant proteins. *$p < 0.05$, **$p < 0.01$, ****$p < 0.001$.

anti-PEG IgG antibodies detected in statistically greater amounts than PBS controls, yielding antibody levels that were ~10^3 lower than the positive control, PEG-KLH (12,900–133,100 U/mL anti-PEG IgG).[41] It is noteworthy that acute anti-PEG responses are not generated by single or double administrations, regardless of PR architecture.

PR Corona Proteomics. PR protein corona formation was studied by incubating the PR with human serum, followed by centrifugal isolation and proteomic analysis of the PR-bound proteins by LC/MS. Total protein deposition and corona compositions varied substantially across PR architectures (Figure 4). The effect was less obvious for total accumulated protein, although on average the more highly threaded PR appear to adsorb less serum protein (Figure 4a). To highlight differences in total protein corona composition associated with each PR, the bound components were divided into six respective classes, complement proteins, serum albumin, coagulation proteins, immunoglobulins, lipoproteins, and other blood borne proteins (Figure 4b). By expressing each family as a percentage of the total corona, the comparative data reveal whether PR family members are preferentially acting within a given pathway. A large percentage of complement proteins or immunoglobulins, for instance, would indicate potential for hypersensitivity reactions or accelerated blood clearance.

Notably, the PR library members adsorbed lipoproteins as the most significant fraction of the protein corona (39–70%) in all cases except for PR4 (26%) (Figure 4b). Lipoproteins made up 56.4 and 70.1% of the coronas of PR1 and PR2, respectively. Because lipoproteins shuttle cholesterol through the blood-stream as a lipid–protein complex, their extensive association is likely driven by interaction with the PR cholesterol end-caps. Because PR1 and PR2 have significantly longer PEG blocks than the other PR architectures, it is possible that increased extension of cholesterol end-caps away from the PR core region is beneficial for lipoprotein association.

PR5 bound the greatest amount of serum albumin, accounting for 17.1% of total protein corona composition on average, potentially accounting for the longer circulation of this construct (Figure 4b). The numerous exposed sugar residues of this more highly threaded PR may also contribute to a slightly increased immunoglobulin deposition. All PRs accumulated between 12 and 25% corona proteins from the coagulation and complement pathways. In all cases, the amount of adsorbed complement proteins were higher, likely because of the surface exposed glycosidic alcohols present on the CD macrocycles.[47]

The largest single protein class on the surface of PR4 is the group of "other" proteins (Figure 4b). Within this group, transthyretin (TTR) made up such a large portion of the adsorbed protein corona on PR4 that it alone was responsible for ~36.9% of the total protein corona content. TTR is an amyloidogenic protein known to drive protein aggregation when partially denatured.[48] If this denaturation and aggregation is being preferentially driven by contact with PR4, the corresponding increase in PR size could promote deposition in lung microcapillaries, providing a possible explanation for the observed lung tissue tropism (Figure 2b). The top 10 proteins on the surface of each PR are listed in Figure 4c. Despite their differences in physiochemical properties, the similarity in HP-β-CD/Pluronic PR chemical composition appears to be driving the recruitment of common proteins.

Several individual proteins within the corona were found to significantly change their abundances ($p < 0.05$) between the PR scaffolds. Proteins that generally make up high-density lipoprotein were highly represented on PR1 and PR2 (Figure S11). Notably, PR 3–5 adsorb less abundant lipoproteins, for example, ApoF and ApoJ, found in low-density lipoprotein. Additionally, the coronas of PR1 and PR2 contain significantly

DOI: 10.1021/acs.biomac.6b00508
Biomacromolecules 2016, 17, 2777–2786

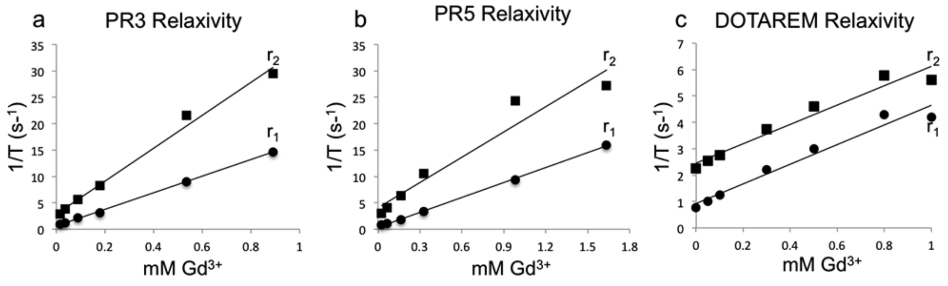

d

	R1 (s^{-1})	R2 (s^{-1})
DOTAREM	3.7	3.7
PR3	16	31
PR5	9.5	16

Figure 5. Relaxivity measurements at 7 T. (a) PR3 and (b) PR5 enhance r_1 relaxivity greater than (c) DOTAREM control.

higher amounts of complement components that contribute to the terminal membrane attack complex, including complement C5, C6, C7, and C8, whereas all the other PR accumulate classical pathway component C4 within their coronas. As discussed above, PR4 shows vastly enhanced levels of TTR. A full list of the protein corona compositions and proportions appear in File 1.

PR Magnetic Resonance Imaging Contrast Enhancement. Given that PRs are able carry Gd^{3+}/DO3A and circulate for extended periods, we investigated their potential as MR contrast agents. Increased pharmacokinetics of macromolecular contrast agents could provide clinical benefit for cardiovascular and tumor imaging relative to current MRI contrast agents that rapidly clear from blood by renal elimination.[49] With this in mind, two PR with the longest circulation times, PR3 and PR5, were evaluated for their MR contrast enhancement properties. Relaxivity measurements of PR3, PR5, and DOTAREM (control) gave r_1 values of ~16, ~9.5, and ~3.7 mM^{-1} s^{-1}, respectively at 7T (Figure S12), values that are very similar to PR1 (Figure 5),[30] and ionic relaxivity enhancements of 4.3 (PR3) and 2.6 (PR5) relative to DOTAREM. A combination of PR rodlike rigidity, imparted by rotaxanation, and a slower tumbling rate, imparted by the increase in molecular weight, are likely responsible for the observed relaxivity enhancements. Further study will be necessary to reveal the relationships between PR physiochemical properties and ionic relaxivity.

CONCLUSIONS

Analyses of PR biodistribution, circulation time, excretion, toxicity, protein corona composition, and MRI contrast capabilities were performed in mice as a function of PR physiochemical properties. We have shown that more highly threaded PR circulate longer and deposit preferentially in the liver compared to PR with lower degrees of threading that leave circulation quickly and deposit to a greater extent in the lungs. More highly threaded PRs then are able to pass through the lungs for final deposition into the liver for hepatobiliary excretion. Differential deposition properties of this type may be useful for designing PR that specifically target lung or liver tissue. In depth study of these effects using PR materials isolated with individual HP-β-CD copy numbers will be necessary to determine the exact trends and limits to these relationships. PR do not exhibit hemolytic potential, do not affect the growth rate of mice after multiple dosings, do not generate an acute anti-PEG IgG response, and do not affect the natural serum chemistry in ways that would be indicative of organ damage.

In contrast, PR bearing different polymer cores do exhibit differential recruitment of serum proteins. Total protein accumulation appears to be reduced for PR of higher threading efficiencies. In all cases, it was observed that PR recruit significant amounts of lipoproteins, which may help promote PR cell uptake through receptor-mediated endocytosis upon binding to relevant surface receptors. Lipoprotein concentrations appear to be dictated by the central copolymer, potentially revealing that increased PEG length aids in lipoprotein association through the PR cholesterol end-caps. Finally, PR are capable of enhancing MRI contrast and show the potential to make attractive MRI diagnostic candidates. These findings show that PR biological performances may be tunable with respect to their physiochemical properties, suggesting that the synthetic design of these materials can be adapted to the specific needs of the target biomedical application.

ASSOCIATED CONTENT

Supporting Information

The Supporting Information is available free of charge on the ACS Publications website at DOI: 10.1021/acs.biomac.6b00508.

PR NMR characterization, additional serum chemistry, proteomics principle component analysis and heatmap, and PR MRI relaxivity images(PDF)

Full table of PR associated proteins is available in supplemental file 1(XLSX)

AUTHOR INFORMATION

Corresponding Author

*E-mail: davethom@purdue.edu. Phone: 1-765-494-0386.

Author Contributions

C.J.C., D.T., and Z.R.L. conceived the experiments. C.J.C. wrote the manuscript. Y.M. and B.L. synthesized and characterized PR materials. Y.M. and B.L. analyzed PR relaxivity. N.A. took ICP-MS measurements of MR agents. C.J.C. and C.S. processed tissue samples. C.J.C. conducted in vitro toxicity experiments and analyzed PK, toxicity, and proteomics data. S.T.A., B.E., and C.J.C. conducted animal experiments.

DOI: 10.1021/acs.biomac.6b00508
Biomacromolecules 2016, 17, 2777−2786

Notes

The authors declare no competing financial interest.

■ ACKNOWLEDGMENTS

We would like to acknowledge the Purdue Biological Evaluation Shared Resource (BE-SR) for all animal studies as well as the Purdue Proteomics Core, particularly Dr. Lake Paul, Victoria Hedrick, and Dr. Tiago Sobreira. We would also like to thank the Purdue Mass Spectrometry core, especially Dr. Karl Wood and Arlene Rothwell-Pearl. Financial support from the Ara Parsegian Medical Research Foundation, the National Institutes of Health (EB017921), the Purdue University Center for Cancer Research (NIH P30 CA023168; animal husbandry, NMR and MS data), and the Indiana Clinical and Translational Sciences Institute Core Pilot Funding Grant (UL1TR001108; MRI data) is also gratefully acknowledged.

■ REFERENCES

(1) Weber, S.; Zimmer, A.; Pardeike, J. Solid Lipid Nanoparticles (SLN) and Nanostructured Lipid Carriers (NLC) for pulmonary application: A review of the state of the art. *Eur. J. Pharm. Biopharm.* **2014**, *86*, 7−22.

(2) Feng, L.; Zhu, C.; Yuan, H.; Liu, L.; Lv, F.; Wang, S. Conjugated polymer nanoparticles: preparation, properties, functionalization and biological applications. *Chem. Soc. Rev.* **2013**, *42*, 6620−6633.

(3) Lee, J. E.; Lee, N.; Kim, T.; Kim, J.; Hyeon, T. Multifunctional mesoporous Silica nanocomposite nanoparticles for theranostic applications. *Acc. Chem. Res.* **2011**, *44*, 893−902.

(4) Albanese, A.; Tang, P. S.; Chan, W. C. W. The Effect of Nanoparticle Size, Shape, and Surface Chemistry on Biological Systems. *Annu. Rev. Biomed. Eng.* **2012**, *14*, 1−16.

(5) Geng, Y.; Dalhaimer, P.; Cai, S.; Tsai, R.; Tewari, M.; Minko, T.; Discher, D. E. Shape effects of filaments versus spherical particles in flow and drug delivery. *Nat. Nanotechnol.* **2007**, *2*, 249−255.

(6) Smith, B. R.; Kempen, P.; Bouley, D.; Xu, A.; Liu, Z.; Melosh, N.; Dai, H.; Sinclair, R.; Gambhir, S. S. Shape matters: Intravital microscopy reveals surprising geometrical dependence for nanoparticles in tumor models of extravasation. *Nano Lett.* **2012**, *12*, 3369−3377.

(7) Ernsting, M. J.; Murakami, M.; Roy, A.; Li, S.-D. Factors controlling the pharmacokinetics, biodistribution and intratumoral penetration of nanoparticles. *J. Controlled Release* **2013**, *172*, 782−794.

(8) Bertrand, N.; Leroux, J.-C. The journey of a drug-carrier in the body: An anatomo-physiological perspective. *J. Controlled Release* **2012**, *161*, 152−163.

(9) Dobrovolskaia, M. A.; Aggarwal, P.; Hall, J. B.; McNeil, S. E. Preclinical studies to understand nanoparticle interaction with the immune system and its potential effects on nanoparticle biodistribution. *Mol. Pharmaceutics* **2008**, *5*, 487−495.

(10) Yu, K.; Lai, B. F. L.; Foley, J. H.; Krisinger, M. J.; Conway, E. M.; Kizhakkedathu, J. N. Modulation of complement activation and amplification on nanoparticle surfaces by glycopolymer conformation and chemistry. *ACS Nano* **2014**, *8*, 7687−703.

(11) Hamad, I.; Al-Hanbali, O.; Hunter, A. C.; Rutt, K. J.; Andresen, T. L.; Moghimi, S. M. Distinct polymer architecture mediates switching of complement activation pathways at the nanosphere−serum interface: Implications for stealth nanoparticle engineering. *ACS Nano* **2010**, *4*, 6629−6638.

(12) Soo Choi, H.; Liu, W.; Misra, P.; Tanaka, E.; Zimmer, J. P.; Itty Ipe, B.; Bawendi, M. G.; Frangioni, J. V. Renal clearance of quantum dots. *Nat. Biotechnol.* **2007**, *25*, 1165−1170.

(13) Alexis, F.; Pridgen, E.; Molnar, L. K.; Farokhzad, O. C. Factors affecting the clearance and biodistribution of polymeric nanoparticles. *Mol. Pharmaceutics* **2008**, *5*, 505−515.

(14) Yang, S.-T.; Wang, X.; Jia, G.; Gu, Y.; Wang, T.; Nie, H.; Ge, C.; Wang, H.; Liu, Y. Long-term accumulation and low toxicity of single-walled carbon nanotubes in intravenously exposed mice. *Toxicol. Lett.* **2008**, *181*, 182−189.

(15) Barbier, O.; Jacquillet, G.; Tauc, M.; Cougnon, M.; Poujeol, P. Effect of heavy metals on, and handling by, the kidney. *Nephron Physiol.* **2005**, *99*, 105−110.

(16) Aillon, K. L.; Xie, Y.; El-Gendy, N.; Berkland, C. J.; Forrest, M. L. Effects of nanomaterial physicochemical properties on in vivo toxicity. *Adv. Drug Delivery Rev.* **2009**, *61*, 457−466.

(17) Monopoli, M. P.; Bombelli, F. B.; Dawson, K. A. Nanobiotechnology: Nanoparticle coronas take shape. *Nat. Nanotechnol.* **2011**, *6*, 11−12.

(18) Barrán-Berdón, A. L.; Pozzi, D.; Caracciolo, G.; Capriotti, A. L.; Caruso, G.; Cavaliere, C.; Riccioli, A.; Palchetti, S.; Laganà, A. Time evolution of nanoparticle−protein corona in human plasma: Relevance for targeted drug delivery. *Langmuir* **2013**, *29*, 6485−6494.

(19) Walczyk, D.; Bombelli, F. B.; Monopoli, M. P.; Lynch, I.; Dawson, K. A. What the cell "sees" in bionanoscience. *J. Am. Chem. Soc.* **2010**, *132*, 5761−5768.

(20) Monopoli, M. P.; Walczyk, D.; Campbell, A.; Elia, G.; Lynch, I.; Baldelli Bombelli, F.; Dawson, K. A. Physical−chemical aspects of protein corona: Relevance to in vitro and in vivo biological impacts of nanoparticles. *J. Am. Chem. Soc.* **2011**, *133*, 2525−2534.

(21) Eigenheer, R.; Castellanos, E. R.; Nakamoto, M. Y.; Gerner, K. T.; Lampe, A. M.; Wheeler, K. E. Silver nanoparticle protein corona composition compared across engineered particle properties and environmentally relevant reaction conditions. *Environ. Sci.: Nano* **2014**, *1*, 238−247.

(22) Tenzer, S.; Docter, D.; Rosfa, S.; Wlodarski, A.; Kuharev, J.; Rekik, A.; Knauer, S. K.; Bantz, C.; Nawroth, T.; Bier, C.; Sirirattanapan, J.; Mann, W.; Treuel, L.; Zellner, R.; Maskos, M.; Schild, H.; Stauber, R. H. Nanoparticle size is a critical physicochemical determinant of the human blood plasma corona: A comprehensive quantitative proteomic analysis. *ACS Nano* **2011**, *5*, 7155−7167.

(23) Harada, A.; Li, J.; Kamachi, M. The molecular necklace: A rotaxane containing many threaded α-cyclodextrins. *Nature* **1992**, *356*, 325−7.

(24) Kabanov, A. V.; Lemieux, P.; Vinogradov, S.; Alakhov, V. Pluronic block copolymers: novel functional molecules for gene therapy. *Adv. Drug Delivery Rev.* **2002**, *54*, 223−233.

(25) Ooya, T.; Mori, H.; Terano, M.; Yui, N. Synthesis of a biodegradable polymeric supramolecular assembly for drug delivery. *Macromol. Rapid Commun.* **1995**, *16*, 259−263.

(26) Loethen, S.; Ooya, T.; Choi, H. S.; Yui, N.; Thompson, D. H. Synthesis, characterization, and pH-Triggered dethreading of α-cyclodextrin-poly(ethylene glycol) polyrotaxanes bearing cleavable endcaps. *Biomacromolecules* **2006**, *7*, 2501−2506.

(27) Collins, C. J.; McCauliff, L. A.; Hyun, S.-H.; Zhang, Z.; Paul, L. N.; Kulkarni, A.; Zick, K.; Wirth, M.; Storch, J.; Thompson, D. H. Synthesis, characterization, and evaluation of pluronic-based β-cyclodextrin polyrotaxanes for mobilization of accumulated cholesterol from Niemann-Pick Type C fibroblasts. *Biochemistry* **2013**, *52*, 3242−3253.

(28) Kulkarni, A.; DeFrees, K.; Schuldt, R. A.; Hyun, S.-H.; Wright, K. J.; Yerneni, C. K.; VerHeul, R.; Thompson, D. H. Cationic α-cyclodextrin:poly(ethylene glycol) polyrotaxanes for siRNA delivery. *Mol. Pharmaceutics* **2013**, *10*, 1299−1305.

(29) Mondjinou, Y. A.; McCauliff, L. A.; Kulkarni, A.; Paul, L.; Hyun, S.-H.; Zhang, Z.; Wu, Z.; Wirth, M.; Storch, J.; Thompson, D. H. Synthesis of 2-hydroxypropyl-β-cyclodextrin/pluronic-based polyrotaxanes via heterogeneous reaction as potential Niemann-Pick Type C therapeutics. *Biomacromolecules* **2013**, *14*, 4189−4197.

(30) Zhou, Z.; Mondjinou, Y.; Hyun, S.-H.; Kulkarni, A.; Lu, Z.-R.; Thompson, D. H. Gd^{3+}-1,4,7,10-tetraazacyclododecane-1,4,7-triacetic-2-hydroxypropyl-β-cyclodextrin/pluronic polyrotaxane as a long circulating high relaxivity MRI contrast agent. *ACS Appl. Mater. Interfaces* **2015**, *7*, 22272−22276.

(31) Yu, S.; Yuan, J.; Shi, J.; Ruan, X.; Wang, Y.; Gao, S.; Du, Y. One-pot synthesis of water-soluble, β-cyclodextrin-based polyrotaxanes in a

DOI: 10.1021/acs.biomac.6b00508
Biomacromolecules 2016, 17, 2777−2786

homogeneous water system and its use in bio-applications. *J. Mater. Chem. B* **2015**, *3*, 5277−5283.
(32) Yu, S.; Zhang, Y.; Wang, X.; Zhen, X.; Zhang, Z.; Wu, W.; Jiang, X. Synthesis of paclitaxel-conjugated β-cyclodextrin polyrotaxane and its antitumor activity. *Angew. Chem., Int. Ed.* **2013**, *52*, 7272−7277.
(33) Yui, N.; Ooya, T.; Kumeno, T. Effect of biodegradable polyrotaxanes on platelet activation. *Bioconjugate Chem.* **1998**, *9*, 118−125.
(34) Park, H.; Bae, J.; Park, K.; Ooya, T.; Yui, N.; Jang, J.-H.; Han, D.; Shin, J.-W. Surface modification of polyurethane using sulfonated PEG crafted polyrotaxane for improved biocompatibility. *Macromol. Res.* **2006**, *14*, 73−80.
(35) Joung, Y. K.; Sengoku, Y.; Ooya, T.; Park, K. D.; Yui, N. Anticoagulant supramolecular-structured polymers: Synthesis and anticoagulant activity of taurine-conjugated carboxyethylester-polyrotaxanes. *Sci. Technol. Adv. Mater.* **2005**, *6*, 484−490.
(36) Fujita, H.; Ooya, T.; Kurisawa, M.; Mori, H.; Terano, M.; Yui, N. Thermally switchable polyrotaxane as a model of stimuli-responsive supramolecules for nano-scale devices. *Macromol. Rapid Commun.* **1996**, *17*, 509−515.
(37) Harkness, J. E.; Wagner, J. E. *The Biology and Medicine of Rabbits and Rodents*, 3rd ed.; Lea & Febiger: Philadelphia, PA, 1989.
(38) Merlitz, H.; Cui, W.; Su, C.-F.; Wu, C.-X.; Sommer, J.-U. Grafted polyrotaxanes: Scaling theory and molecular dynamics simulations. *Macromolecules* **2014**, *47*, 4110−4117.
(39) Frijlink, H. W.; Visser, J.; Hefting, N. R.; Oosting, R.; Meijer, D. K.; Lerk, C. F. The pharmacokinetics of β-cyclodextrin and hydroxypropyl-β-cyclodextrin in the rat. *Pharm. Res.* **1990**, *7*, 1248−1252.
(40) Liu, B.; Ramirez, C. M.; Miller, A. M.; Repa, J. J.; Turley, S. D.; Dietschy, J. M. Cyclodextrin overcomes the transport defect in nearly every organ of NPC1 mice leading to excretion of sequestered cholesterol as bile acid. *J. Lipid Res.* **2010**, *51*, 933−944.
(41) Life Diagnostics, Mouse Anti-PEG IgG ELISA Kit, Catalog # PEGG-1, Instructions, http://www.lifediagnostics.com/wp-content/uploads/PEGG-1.pdf.
(42) Cacheris, W. P.; Quay, S. C.; Rocklage, S. M. The relationship between thermodynamics and the toxicity of gadolinium complexes. *Magn. Reson. Imaging* **1990**, *8*, 467−481.
(43) Gould, S.; Scott, R. C. 2-Hydroxypropyl-β-cyclodextrin (HP-β-CD): A toxicology review. *Food Chem. Toxicol.* **2005**, *43*, 1451−1459.
(44) Minetti, M.; Agati, L.; Malorni, W. The microenvironment can shift erythrocytes from a friendly to a harmful behavior: pathogenetic implications for vascular diseases. *Cardiovasc. Res.* **2007**, *75*, 21−28.
(45) Owens, D. E., III; Peppas, N. A. Opsonization, biodistribution, and pharmacokinetics of polymeric nanoparticles. *Int. J. Pharm.* **2006**, *307*, 93−102.
(46) Ishihara, T.; Takeda, M.; Sakamoto, H.; Kimoto, A.; Kobayashi, C.; Takasaki, N.; Yuki, K.; Tanaka, K.-i.; Takenaga, M.; Igarashi, R.; Maeda, T.; Yamakawa, N.; Okamoto, Y.; Otsuka, M.; Ishida, T.; Kiwada, H.; Mizushima, Y.; Mizushima, T. Accelerated blood clearance phenomenon upon repeated injection of PEG-modified PLA-nanoparticles. *Pharm. Res.* **2009**, *26*, 2270−2279.
(47) Reddy, S. T.; van der Vlies, A. J.; Simeoni, E.; Angeli, V.; Randolph, G. J.; O'Neil, C. P.; Lee, L. K.; Swartz, M. A.; Hubbell, J. A. Exploiting lymphatic transport and complement activation in nanoparticle vaccines. *Nat. Biotechnol.* **2007**, *25*, 1159−1164.
(48) Hamilton, J.; Benson, M. Transthyretin: a review from a structural perspective. *Cell. Mol. Life Sci.* **2001**, *58*, 1491−1521.
(49) Mohs, A. M.; Lu, Z.-R. Gadolinium (III)-based blood-pool contrast agents for magnetic resonance imaging: status and clinical potential. *Expert Opin. Drug Delivery* **2007**, *4*, 149−64.

DOI: 10.1021/acs.biomac.6b00508
Biomacromolecules 2016, 17, 2777−2786